LUND UNIVERSITY

Dielectric Characterization of Soil Samples by Microwave Measurements

Santos, Telmo; Johansson, Anders J; Tufvesson, Fredrik

2009

Total number of authors:
3

Dielectric Characterization of Soil Samples by Microwave Measurements

Telmo Santos, Anders J. Johansson and Fredrik Tufvesson

Dept. of Electrical and Information Technology
LUND UNIVERSITY

Abstract

Northern high-latitude wetlands are well known to seasonally emit methane gas into the atmosphere, and therefore contribute to greenhouse effects. While these gas emissions are well documented, their causes are not well understood. The method described in this work can be used to analyze the changes happening in the soil during gas emissions, and therefore help the understanding of the sub-surface gas dynamics.

We have monitored a sample of peat soil through an artificial freezing and thawing cycle, using both a gas detector to measure the methane flux at the soil surface and a vector network analyzer to measure the transmission of microwaves through the soil. It was observed that the results from the two measurement approaches had a very good match under specific microwave signal conditions. In addition, from the microwave measured data, the dielectric properties of the soil and the volumetric fractions of its constituents were also calculated based on a dielectric mixing model.

1 Introduction

Methane (CH_4) is a natural atmospheric gas with the property of absorbing infra-red radiation. This property makes it a greenhouse gas, and in this category, methane is more than 20 times stronger than carbon dioxide (CO_2) [1]. In addition, following water vapor and carbon dioxide, methane is the most abundant greenhouse gas in the troposphere [2]. The methane present in the atmosphere is due to both human activity and natural causes, and the northern high-latitude wetlands contribute to 72% of all the natural methane emissions [2]. Concern is also given to the eventual thawing of the permafrost in these locations, and the consequent release of the carbon their deposited, since this could lead to a positive feedback effect on the global temperature.

The Zackenberg Ecological Research Operations (ZERO) research station at Zackenberg, Greenland, is located in such wetlands, and part of its activities include the monitoring of gas emissions from the soil. In 2007, besides the expected methane emissions during the spring, a large methane burst was also detected during the autumn, on the onset of freezing [3]. The integral of emissions during the freeze-in period was approximately equal to the amount of methane emitted during the entire summer season. This finding triggered new interest on the understanding of how the freezing/thawing processes influence gas emissions from the soil.

In this work, we aim to cast some light on the unknown gas dynamics happening within the soil before and during the gas emissions. In order to do so, we monitored a sample of peat soil while it was artificially frozen and thawed in a controlled laboratory environment. Our work is novel in that the monitoring was done both at the surface and at the sub-surface level, using two completely independent measurement techniques: methane flux measurements and microwave measurements, respectively. From the collected data, we calculated the bulk dielectric constant of the soil. The soil was then modeled as being composed of a *gas*, a *water* and a *solid* part, and the corresponding volumetric fractions were computed based on a dielectric mixing model.

The reminder of the paper is organized as follows. First, in Section 2 we present the background theory in which we base our calculations of the dielectric constant and volumetric fractions. In Section 3 we describe the measurement setup and give insight on how undesired diffraction and reflection effects can be minimized. In Section 4 we describe the post-processing applied to the data, and in Section 5 we present and discuss the measurement results. Lastly, in Section 6 we list the findings and propose future work.

2 Background Theory

2.1 Propagation Through a Dielectric Slab

In this work we analyzed the measurements of microwave signals transmitted through, and reflected from, a sample of soil. These effects can be well described mathematically by the expressions of transmission and reflection coefficients of an infinite dielectric slab [4, 5, 6]. For the case of a slab with length L, and considering free-space around the slab, the transmission coefficient is defined by

$$S_{21}(f) = |S_{21}(f)| e^{j\phi_{21}} = \frac{(1 - R^2) e^{-\gamma L}}{1 - R^2 e^{-2\gamma L}} \tag{1}$$

and the corresponding reflection coefficient is

$$S_{11}(f) = |S_{11}(f)| e^{j\phi_{11}} = \frac{(1 - e^{-2\gamma L}) R}{1 - R^2 e^{-2\gamma L}}. \tag{2}$$

where R is the field reflection coefficient (defined ahead). The propagation constant of the dielectric-filled slab γ, is defined in terms of the attenuation coefficient α and the phase factor β as

$$\gamma = \alpha + j\beta = \frac{2\pi}{\lambda_0} \sqrt{-\varepsilon_r} \tag{3}$$

where $\frac{2\pi}{\lambda_0} = k_0$ is the wavenumber in free space, λ_0 is the free space wavelength and ε_r is the relative complex dielectric permittivity of the sample which is composed by a real and imaginary part

$$\varepsilon_r = \varepsilon' - j\varepsilon''. \tag{4}$$

The real part ε' is related with the *propagation speed* as $v = c/\sqrt{\varepsilon'}$, where c is the speed of light in vacuum, whereas ε'' is related with the *attenuation* through the dielectric material. The relative complex dielectric permittivity[1] ε_r is related with the effective dielectric permittivity ε by

$$\varepsilon = \varepsilon_r \varepsilon_0, \tag{5}$$

where ε_0 is the dielectric constant in free space. From the above, ε' and ε'' can also be formulated as

$$\varepsilon' = \left(\frac{1}{k_0}\right)^2 \left[-\left(\alpha^2 - \beta^2\right)\right] \tag{6}$$

$$\varepsilon'' = \left(\frac{1}{k_0}\right)^2 (2\alpha\beta). \tag{7}$$

The field reflection coefficient R is given in terms of Z_0, the intrinsic impedance of free space, and Z is the characteristic impedance of the dielectric-filled slab

$$R = \frac{Z - Z_0}{Z + Z_0}. \tag{8}$$

---

[1]Throughout the rest of the paper we drop the words "relative complex" and refer to ε_r simply as "dielectric permittivity" or "dielectric constant."

These impedances are given by

$$Z = \frac{j\omega\mu_0}{\gamma} = \frac{2\pi\eta_0}{\lambda_0} \cdot \frac{\beta\left(1 + j\alpha/\beta\right)}{\alpha^2 + \beta^2} \tag{9}$$

$$Z_0 = \mu_0 c = \sqrt{\frac{\mu_0}{\varepsilon_0}} \tag{10}$$

$$\mu_0 = 4\pi \times 10^{-7} \tag{11}$$

$$\varepsilon_0 = \frac{1}{\mu_0 c^2} \tag{12}$$

$$c = 2.9979 \times 10^8, \tag{13}$$

where $\omega = 2\pi f$ is the angular velocity at frequency f and μ_0 is the permeability of free space.

2.2 Dielectric Mixing Model

Soil samples such as peat are generally composed of different materials, e.g., earth, gases and water. Hence, the corresponding measured dielectric constant will be dependent on the electric properties of the different constituents. One way to describe the bulk (or total) dielectric constant is by using a so called *dielectric mixing model*. A well accepted mixing model is the one proposed by Lichtenecker [7]

$$\varepsilon_{\text{bulk}}^{\alpha} = \sum_i \Theta_i \varepsilon_i^{\alpha} \tag{14}$$

$$\sum_i \Theta_i = 1 \tag{15}$$

where ε_i is the dielectric constant of the i:th constituent and Θ_i is the corresponding volumetric fraction. The exponent α can range from -1 to 1, and defines the arrangement of the constituents to each other. The theoretical value of α for an homogeneous mixture is 0.5, which is the one used in this work. Lichteneckers mixture formulae (15) was originally derived in an empirical way, but was latter also derived theoretically [8].

2.3 Debye Theory of Dielectric Relaxation

Single materials are well described by the Debye theory of dielectric relaxation [9]. It assigns three parameters to each material, which describe how electric dipoles behave when excited by different frequencies

$$\varepsilon_r(w) = \varepsilon_\infty + \frac{\varepsilon_{\text{dc}} - \varepsilon_\infty}{1 + jw\tau} - j\frac{\sigma}{w}. \tag{16}$$

ε_{dc} represents the static dielectric permittivity, ε_∞ is the permittivity at infinitely high frequencies and τ is the relaxation time of the material. The latter term, containing the electrical conductivity σ, can here be neglected since it diminishes at high frequencies. In this work, we use the Debye theory to describe the frequency dependent dielectric constant of water as is commonly done in the literature, e.g., [10]. The representation of both real and imaginary parts of the dielectric constant based on Debye theory are given in Fig. 1.

3 Measurement Setup and Equipment

The measurement campaign consisted in the monitoring of a sample of peat soil during freezing and thawing processes. A soil sample was collected from Fäjemyr, Skåne, Sweden (56°15′N, 13°33′E) and stored in a plastic container with dimensions $36 \times 27 \times 22$ cm. The sampling
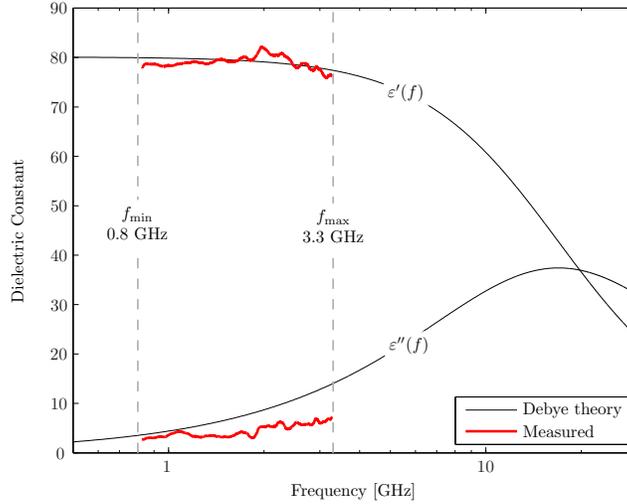
Figure 1: Theoretical and measured dielectric constant of water at 20° C.

site was chosen for its similarities with Greenland regarding soil properties. In addition, the height of the soil sample agrees with the height of the layer of soil above the permafrost in Zackenberg, Greenland. As a preparation for the experiment, the peat soil was incubated for a period of four weeks with a constant water level and in an anaerobic environment to ensure that considerable amount of methane was produced and stored in the soil. The container was then carefully transported to a temperature controlled room at the Department of Physical Geography and Ecosystem Analysis, Lund University. In order to induce the freezing process, a cooling device was placed on the top of the container to simulate the top-down natural freezing conditions. The measurement diagram is given in Fig. 2a and the corresponding photo in Fig. 2b. A methane detector was also placed above the soil to measure gas emissions.

Regarding the microwave part of the setup, the transmitter and receiver antennas were placed on the sides of the container, 5 cm away from the container's surface, and the surrounding volume was filled, as much as possible, with radiation absorber material,[2] see Fig. 2a. The measurements were done with a HP8720C vector network analyzer (VNA), which was set to measure the S_{21} and S_{11} parameters successively.

The VNA was configured to measure 1601 regularly spaced frequency points from 0.8 to 3.3 GHz. This frequency range was chosen as a compromise between the characteristics of the antennas, the amplifier and the soil. The intermediate frequency (IF) bandwidth was set to 1000 Hz. A UWB low noise amplifier (LNA), Mini-Circuits model ZVE-8G, with 28 dB of gain and noise figure of 3.5 dB, was connected between the receiver antenna and Port2 of the VNA. The VNA was controlled by a LabVIEW program running on a notebook computer. The antennas used were UWB SkyCross antennas, model SMT-2TO6MB-A.

Both the methane detector and the VNA were set to take one measurement per minute, during a total period of ten days. For the first two days the soil was maintained at room temperature, then the freezing phase was initiated by turning on the cooling device, and at the end of the seventh day, the thawing phase was started by taking the cooling device out of the measurement setup.

---

[2]Section 3.1 gives a detailed justification for the positioning of the antennas and the absorber material.
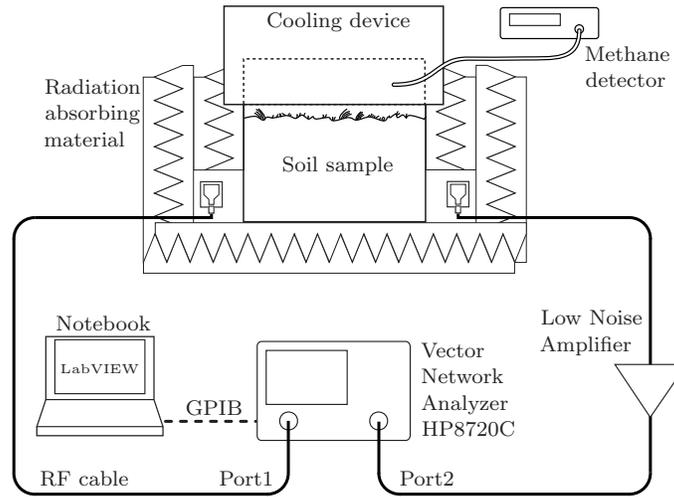
(a) Measurement diagram.
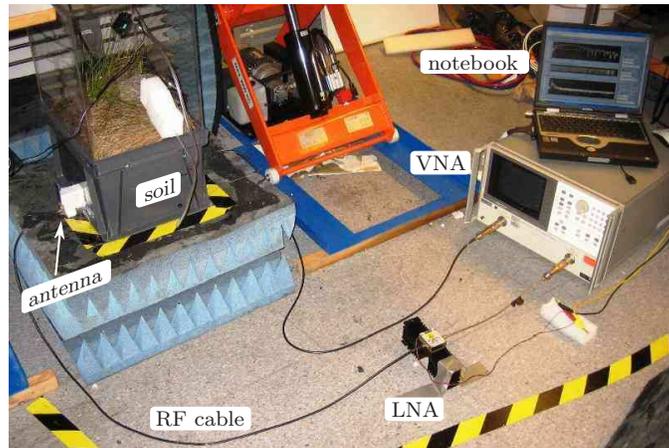
(b) Photo of the measurement setup.

Figure 2: Measurement diagram and corresponding photo at the temperature controlled room, Department of Physical Geography and Ecosystem Analysis, Lund University. Photo taken during the preparation for the measurements.
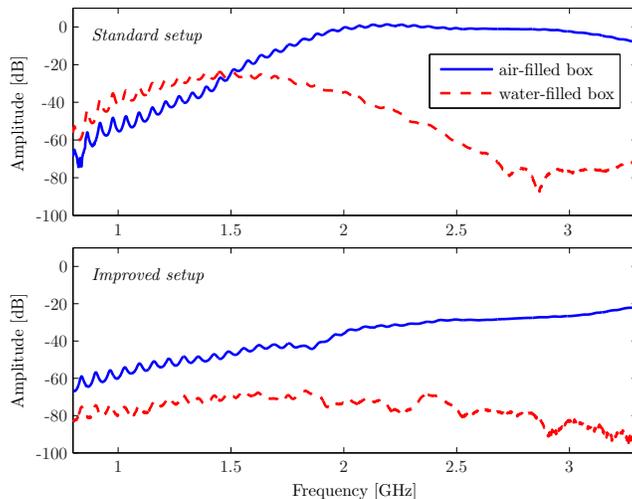
Figure 3: Uncalibrated S_{21} parameter values for standard (upper plot) and improved (lower plot) measurement setup .

3.1 Reducing Undesired Diffraction and Reflection Effects

In order to find the dielectric constant of the material, we assume that the measured S_{21} parameters are well modeled by the transmission equation (1). However, considering the size of our sample, this approximation is only true if the microwave signals arriving at the receiver antenna are only propagating in a straight line from the transmitter antenna, i.e., no additional components exist. In practice, this is impossible to achieve as diffraction components around the sample and reflection components from within the sample will always exist, these are illustrated in Fig. 4. In an effort to minimize these undesired effects we used the following measurement setup:

- Radiation absorbing material was placed on the sides of the plastic box to minimize the diffracted fields.

- The antennas were placed 5 cm away from the box, such that the waves propagating through the sample are more flat, i.e., less spherical, which reduces the strength of the reflection components on the sides of the container. In addition, the antenna mismatch was also reduced since the used antennas are designed for transmission in air.

A representation of the position of the absorbers and the antennas is given in Fig. 2a. In order to quantify the improvements, test measurements were performed considering an empty box and water-filled box, see Fig. 3. From the upper plot, it is visible how strong the diffraction components are. For the lower frequencies, the transmission through water is larger than the transmission in free-space, which is physically impossible if not considering diffraction around the box. By applying the above referred modifications to the measurement setup, the diffracted and reflected fields were generally reduced. This reduction was more significant at the lower frequencies, e.g., at 1 GHz the power was reduced by 40 dB. The results shown in the lower plot of Fig. 3 are more acceptable: the transmission through water is always below transmission in free-space and the difference between the two lines increases with frequency, which agrees with the water property of increasing loss with increasing frequency.

6

4 Data Analysis and Post-Processing

4.1 Calibration

When transmission measurements are done through a sample, the recorded S_{21} parameter includes not only the influence of the sample under test but also the antenna distortions. To correct for this, the measured S_{21} must be calibrated.[3] A simple way to perform this calibration is to do it directly in the frequency domain by a division, as is done by [11],

$$\hat{S}_{21,\text{soil}}(f) = \frac{S_{21,\text{mea.}}(f)}{S_{21,\text{cal.}}(f)}. \tag{17}$$

It is important to note that calibrations performed directly by a division, are only valid under certain conditions. One condition is that the system must be linear and that the introduction of a certain material in the box must not generate additional propagation components, e.g., diffraction and reflection components, as represented in Fig. 4. This in often not the case as materials with $\varepsilon' > 1$ generate diffraction fields around the sample and create new reflected components from within the sample. To find the correction coefficients, $S_{21,\text{cal.}}(f)$, we started by measuring the transmission through an empty box, which contained all the referred non-linearities, $S_{21,\text{free-space}}(f)$. Ideally, $S_{21,\text{cal.}}(f)$ should be the transmission coefficient for when there is no sample at all, such that the antennas would have to be almost touching each other. This is not possible since the two antennas would stop behaving has good radiators due to the coupling between each other. So, our approach is to first measure the empty box (free space), and then "back-rotate" the phase of each one of the frequency points by an amount corresponding to the length of the box L, assuming propagation at the speed of light. In this way, we eliminate the influence of the unwanted free space within the box

$$S_{21,\text{cal.}}(f) = S_{21,\text{free-space}}(f) \cdot e^{j2\pi L f/c} \tag{18}$$

$$= S_{21,\text{free-space}}(f) \cdot e^{jw\tau_0}. \tag{19}$$

where τ_0 is the propagation delay corresponding to a wave traveling at the speed of light through a length of L. This approach also solves an additional problem. The assumption in equation (1) is that the wave impinging on the slab is plane, or lossless, which is not our case since the waves radiated by the antennas are spherical, and therefore lossy. However, the same spherical loss is also measured in $S_{21,\text{free-space}}(f)$, and will therefore be compensated in (17).

It is important to refer that the above described calibration does not replace the internal calibration of the VNA, which corrects for the equipment's internal errors and non-linearities [12]. However, the internal calibration of the VNA is not sufficient since it is not able to correct for the antenna distortions.

4.2 Calculation of the Dielectric Parts ε' and ε''

The calculation of the dielectric constant is not trivial because there is no direct relation between ε' or ε'', and the measured S_{21} parameter. One approach is to use numerical methods. Several iterative numerical methods have been proposed in the literature, in [5] an iterative algorithm based on (6) and (7) is proposed. The drawback of such algorithms is generally the uncertainty off the convergence to the correct solution, which is usually dependent on the initial values. The non-unique solution, i.e., the fact that several values of ε' and ε'' verify (1) and (2), stems from the repetitive nature of a sinusoidal wave.

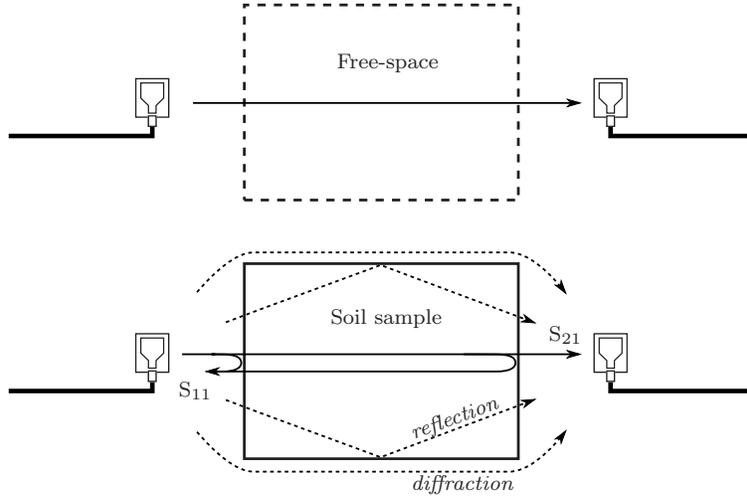[3]Calibration is also referred to as "correction."

Figure 4: Calibration through free-space measurement. The indicated components, e.g., reflection and diffraction, represent the undesired propagation components.

Our approach is based on an exhaustive error minimization search over the values of ε' and ε''. We start by defining the frequency dependent error function as

$$E(f) = \left| \hat{S}_{21,\text{soil}}(f) - \frac{\left(1 - R^2\right)e^{-\gamma L}}{1 - R^2 e^{-2\gamma L}} \right|^2. \tag{20}$$

The corresponding minimization problem is formulated as

$$\{\varepsilon'(f), \varepsilon''(f)\} = \underset{\{\varepsilon',\varepsilon''\}}{\arg\ \min}\ E(f). \tag{21}$$

As mentioned earlier, the solution to (21) is not unique. However, the values of $\varepsilon'(f)$ and $\varepsilon''(f)$ are not expected to change significantly within small frequency bands. We can therefore use the frequency domain to narrow down the number of possible solutions by

$$\{\varepsilon'(f_c), \varepsilon''(f_c)\} = \underset{\{\varepsilon',\varepsilon''\}}{\arg\ \min}\ \int_{f_c-B/2}^{f_c+B/2} E(f)df \tag{22}$$

where B is the band around the center frequency f_c. Since the measured data is restricted to discrete frequency points, we can reformulate (22) with a frequency discrete basis

$$\{\varepsilon'(f_i), \varepsilon''(f_i)\} = \underset{\{\varepsilon',\varepsilon''\}}{\arg\ \min}\ \sum_{i=-N_f/2}^{N_f/2} E(f_{i+n}), \tag{23}$$

where f_i refers to the i:th measured frequency and N_f is the number of consecutive frequencies. In the analysis of the data, N_f was set to 20, which corresponded to a bandwidth of roughly 30 MHz. This bandwidth is acceptable since all soil constituents are expected to have constant dielectric properties within 30 MHz. Even water, the constituent varying the most with frequency, satisfies this condition. Fig. 5 shows the logarithmic error surface based on (22) for both 0.8 and 3.3 GHz when the soil sample was at a temperature below 0°C. It is visible from the figure how challenging it is to choose the correct solution[4] for the higher frequencies since

---

[4]Each possible solution is identified by a "valley" on the error surface, since a "valley" corresponds to the area where the error is minimal.
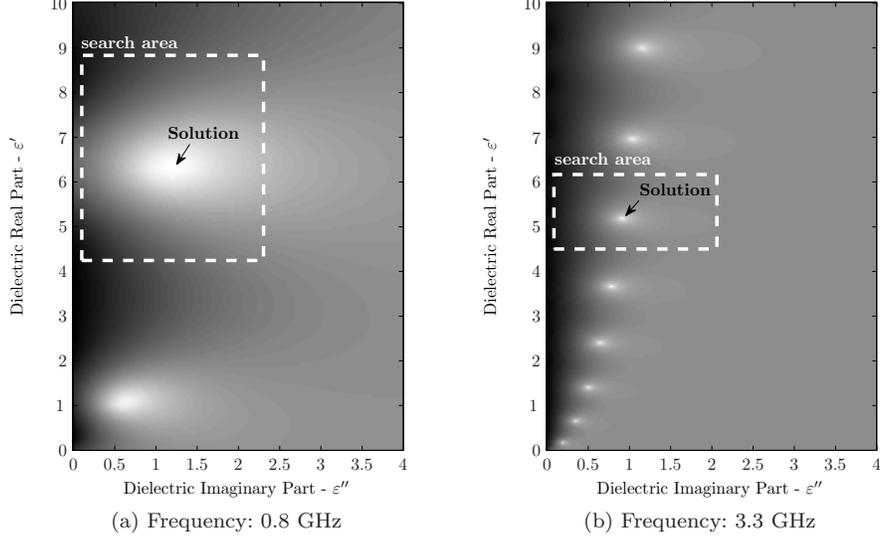
Figure 5: Logarithm of error surface for a soil sample at a temperature below 0°C. The dashed rectangles indicate the grid search area.

the number of solutions increases with increasing frequency. This property is caused by the fact that the amount of phase rotation increases with increasing frequency, when considering the same propagation length.

Our approach to calculate ε' and ε'' for the whole frequency band is the following. First, we find the impulse response of the measured data by means of the IFFT operation. Then, we find the delay, τ_{peak}, corresponding to the strongest peak of the impulse response, and calculate an estimate of ε' by

$$\hat{\varepsilon'} = \left(\frac{c\tau_{\text{peak}}}{L}\right)^2 \tag{24}$$

where c is the speed of light in vacuum. Subsequently, using the error surface corresponding to the lowest frequency, f_1, we find the solution that is closer to $\hat{\varepsilon'}$ by a grid search using (23). For the example shown in Fig. 5a, f_1 is 0.8 GHz and the calculated solution is $\varepsilon'(f_1) = 6.3$ and $\varepsilon''(f_1) = 1.2$. The size of the grid search is depicted in the figure by the dashed rectangle. We then use this solution as a starting point to the calculation of the dielectric constant of the next frequency point, more specifically, the solution of a given frequency becomes the center of the grid search of the next frequency

$$\underbrace{(\varepsilon'(f_n), \varepsilon''(f_n))}_{\text{grid center}} = (\varepsilon'(f_{n-1}), \varepsilon''(f_{n-1})), \quad n > 1. \tag{25}$$

In this way, the solution is tracked until the last frequency point, see Fig. 5b. Since the distance between the adjacent solutions decreases with increasing frequency, the size of the grid search is reduced accordingly, so that only one solution exists within a given grid. In this work, the resolution of the grid search was chosen to ensure an error below 10^{-3} for both ε'' and ε'.

To verify the accuracy of the above described method, measurements were performed with pure water and the calculated dielectric constants were compared with the expected ones based on Debye theory, the results are given in Fig. 1. The deviation between calculated and theoretical curves, appears to increase with increasing frequency for the case of ε'', which indicates that, with the present measurement setup, the calculated results might be underestimating ε'' for the higher frequencies. Nevertheless, the calculations of ε' show a good match with theory.

9

Table 1: Considered dielectric permittivities of the three soil constituents.

	ε_1 gas	ε_2 water	ε_3 solid
ε'	1	Debye (16)	3.150
ε''	0	Debye (16)	0.005

4.3 Dielectric Properties of the Constituent Materials

For the considerations regarding the dielectric properties of the constituent materials, we follow the reasoning presented in [13]. In brief, we model the soil samples by three constituents: *gas*, *water* and *solid*, such that the corresponding volumetric fractions verify

$$\underset{\text{gas}}{\Theta_1} + \underset{\text{water}}{\Theta_2} + \underset{\text{solid}}{\Theta_3} = 1, \quad \Theta_1, \Theta_2, \Theta_3 \geq 0. \tag{26}$$

4.4 Calculation of the Volumetric Fractions

The aim of this work is ultimately to find the value of these three parameters for every time instant.[5] In order to find the three volumetric fractions, we make use of the calculated dielectric constants together with the mixing model described in section 2.2, such that

$$\sqrt{\varepsilon_{\text{calc.}}} = \Theta_1\sqrt{\varepsilon_1} + \Theta_2\sqrt{\varepsilon_2} + \Theta_3\sqrt{\varepsilon_3} \tag{27}$$

where $\varepsilon_{\text{calc.}} = \varepsilon' - j\varepsilon''$ denotes the dielectric constant calculated from the method described in Section 4.2. The values chosen for ε_1, ε_2 and ε_3 are given in Table 1, and the corresponding justification is provided in [13]. Considering Eq. (26), together with the fact that Eq. (27) is complex and therefore needs to be valid independently for the real and imaginary parts, we arrive at a system of three equations

$$\text{Re}\left\{\sqrt{\varepsilon_{\text{calc.}}}\right\} = \text{Re}\left\{\Theta_1\sqrt{\varepsilon_1} + \Theta_2\sqrt{\varepsilon_2} + \Theta_3\sqrt{\varepsilon_3}\right\} \tag{28}$$

$$\text{Im}\left\{\sqrt{\varepsilon_{\text{calc.}}}\right\} = \text{Im}\left\{\Theta_1\sqrt{\varepsilon_1} + \Theta_2\sqrt{\varepsilon_2} + \Theta_3\sqrt{\varepsilon_3}\right\} \tag{29}$$

$$1 = \Theta_1 + \Theta_2 + \Theta_3 \tag{30}$$

from which the three unknowns Θ_1, Θ_2 and Θ_3 can be calculated.

However, the calculation of the volumetric fractions is not straightforward since the above system of equations is non-linear. Following the same approach used for the calculation of ε' and ε'' in Section 4.2, we avoid iterative methods and estimate the three unknowns by means of a fine grid search. By replacing (30) on (28) and (29), the problem can be simplified to a two-dimensional grid search.

5 Results

5.1 Frequency and Time Domain Profiles

The complete data measured by the VNA, after calibration, is illustrated in Fig. 6, in the frequency-domain, and in Fig. 7, in the time-domain.

It is difficult to find an explanation for each and every amplitude variation seen in the figures, however, several general observations can be made. From Fig. 6, at the beginning of the experiment (day zero), when the water was in the liquid state, the amplitude of the transmission decays with increasing frequency. This property is well in line with the predictions from the

---

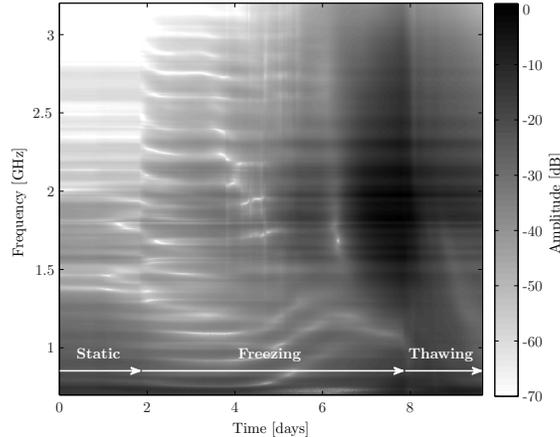[5]The time dependence is not shown in the formulations for clarity.

Figure 6: Measured S_{21} parameter after calibration, for the full ten days of measurements.

Debye model for water. Then, during the freezing phase, while the liquid water was progressively being transformed into solid ice, the higher frequencies progressively became less attenuated (at 3.3 GHz, from day two to day eight, there is an increase in received power of 40 dB). On the other hand, the attenuation of the lower frequencies (e.g., 0.8 GHz) barely changes during the six days of freezing, which also agrees with the Debye model. On the onset of the thawing phase, there is an increase in the volumetric content of liquid water, and the transmission coefficient naturally decreases.

The data presented in Fig. 7, results from applying the IFFT operation to the calibrated S_{21} parameter, and in the figure, there are two aspects worth mentioning: 1) As indicated by the two arrows, the first strong component of the impulse response appears at 8 ns before freezing and at 2 ns after freezing. This indicates that at the start of the measurements, the transmitted pulse[6] propagates mainly through liquid water, and that at day eight the propagation is made mainly through ice. It is also notable that around day four, there are two arriving components with comparable amplitude at delays 3 ns and 8 ns, which point to the fact that, at this instant, there were two separable layers in the soil: a top-frozen layer and a bottom-unfrozen one. 2) Between day six and day eight, a train of amplitude decreasing pulses is visible along the delay domain. This supports the idea that the received power is not only due to one component that propagates through the soil once, but also due to later propagation components which are reflected multiple times from within the soil. This is a characteristic of dielectric slabs with low ε'', as is the case of ice.

5.2 Amplitude and Phase Variations versus Methane Emissions

Regarding methane emissions, these were only detected during the thawing phase, and therefore we now focus our attention to the results from day 7.6 to day 8.6. From Figs. 6 and 7, the amplitude variations in this period appear very smooth. However, when looking with more detail, several sharp small-scale variations (< 1 dB) are visible, see Fig. 8a. These sharp variations are both positive, i.e., increase of amplitude, and negative, i.e., decrease of amplitude. The phase of S_{21} shows similar variations as shown in Fig. 8b.

To better understand the relation between the variations of both the amplitude and phase with the emissions of methane, we plot their time derivatives together for comparison, see Fig. 9. A peak in the derivative of the methane flux, corresponds to a burst emission of methane from

---

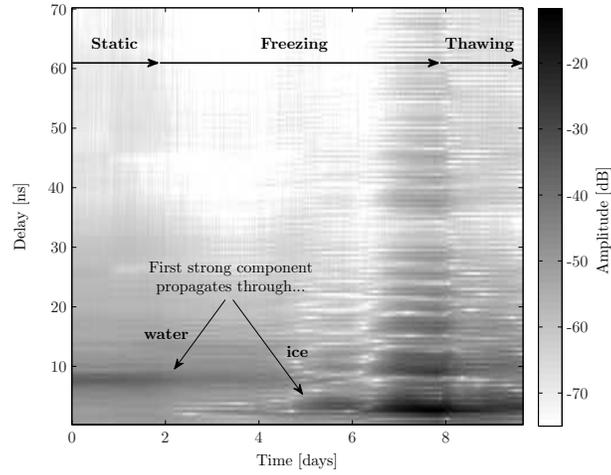[6]By "pulse," we refer to the virtual time-domain "sinc" pulse composed of all the transmitted frequencies.

Figure 7: Impulse response (through IFFT) of the measured S_{21} parameter after calibration, for the full ten days of measurements.

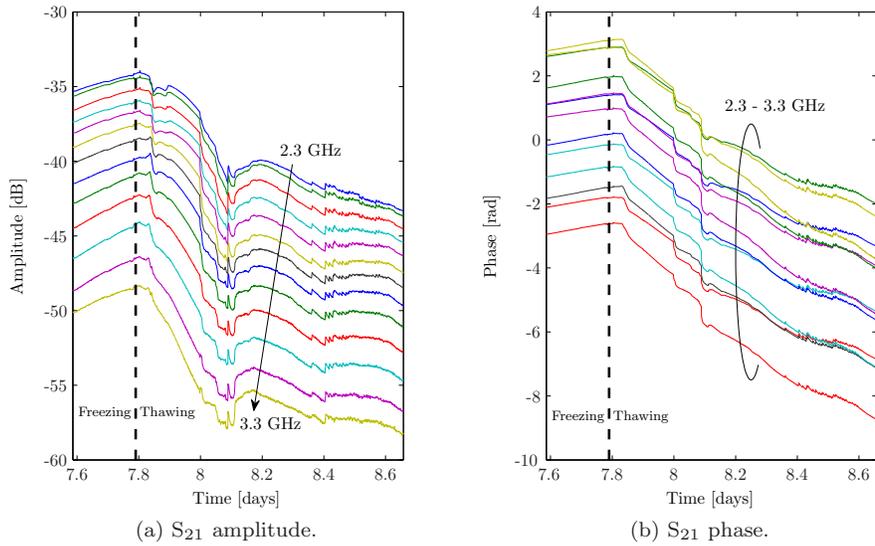(a) S_{21} amplitude.

(b) S_{21} phase.

Figure 8: Measured (uncalibrated) S_{21} parameter between the seventh and eighth day. The vertical dashed line indicates the time instant when the thawing phase was initiated. For clarity the figure only shows the frequency band from 2.3 to 3.3 GHz.
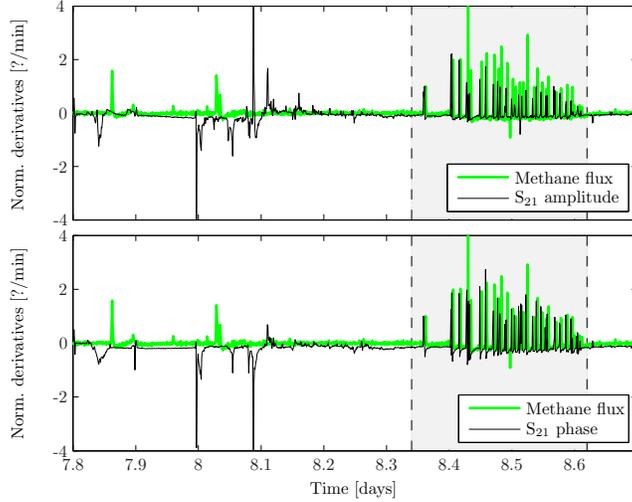
Figure 9: Normalized derivatives of both amplitude and phase of the S_{21} parameter compared against the derivative of methane flux versus time. The normalization was made in relation to the amplitude of the peak at 8.36 days. The shaded area indicates the time window during which the results from the two measurement techniques matched.

the soil sample. These derivatives were computed numerically by the approximation

$$\frac{d}{dt}s(t_n) \approx \frac{s(t_n) - s(t_{n-1})}{t_n - t_{n-1}} \tag{31}$$

where $s(t_n)$ denotes a time dependent function sampled at time instant t_n. In our case, the sampling interval, $t_n - t_{n-1}$ was one minute. To facilitate the comparison, the curves were normalized to the peak amplitude at time instant 8.36 days. The derivatives in both subplots do not show a perfect match, some peaks appear to match well while others don't match at all. However, a more careful observation reveals an interesting characteristic:

at all the instants when both the amplitude and the phase increase, the methane flux at the surface also increases.

The shaded area in Fig. 9, indicates the time window during which the match between the two measurements techniques was very good. Fig. 10, shows the initial part of that time window in detail, for both amplitude and phase. There is also a visible delay of roughly two minutes between the two curves.[7]

It should be noted that a perfect match between the results of the two measurement devices was not expected since these were not measuring the same physical volume. The VNA was measuring the transmission through the soil sample at a sub-surface level, and the methane detector was measuring the gas flux at the surface. Therefore, properties within the sample might change without resulting in any gas emission at the surface.

5.3 Volumetric Fractions and their Interpretation

Finally, we applied the method described in Section 4.2, to calculate the dielectric constant of all the frequencies for the different time instants. The corresponding volumetric fractions were

---

[7]At the time of the measurements, it was not possible to verify whether this delay was caused by the soil itself (a delay between a change in the lower layers of the soil, and the emission of methane at the surface), or if it was caused by a mismatch between the clock of the computer storing the S_{21} parameter and the clock of the computer storing the methane flux.
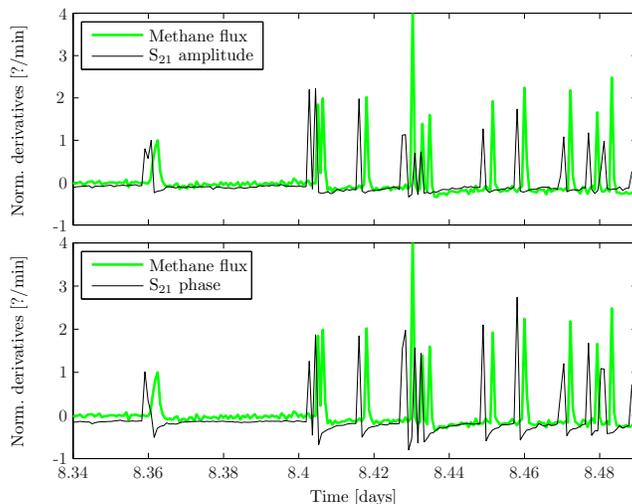
Figure 10: Normalized derivatives of both amplitude and phase of the S_{21} parameter compared against the derivative of methane flux versus time. The time between consecutive samples is one minute.

calculated based on the formulations given in Section 4.4.

Fig. 11 shows the calculated volumetric fractions versus time. The two small subplots give a detail of the volumetric fraction of the solid and gas parts, for the time window when there was a good match between the derivative curves (i.e., the time window of Fig. 10). By comparing the time instants of the methane emissions with the calculated volumetric fractions, it is evident that each emission is characterized by a drop in the content of gas and corresponding increase in the content of the solid part. Furthermore, after each emission, the gas content within the soil appears to slowly increase with time until the next abrupt drop, or gas emission. One possible interpretation for these results is that, due to the depressure caused by the melting of the ice, the methane is allowed to move within the soil, where it accumulates in localized air pockets, until a channel to the surface becomes available, triggering the methane emission. It is however important to be careful when interpreting these results, since these are only taken from a single experiment.

6   Conclusions and Future Work

In this work we have performed a laboratory experiment on a sample of peat soil, where the temperature was controlled to induce freezing, and subsequently thawing, in a sample of peat soil. The aim was to simulate the yearly temperature changes experienced by the soil in Greenland at the onset of the autumn and spring, respectively. The microwave and methane measurements showed a good correlation during the time when both the amplitude and phase of the transmission coefficients had a positive derivative. This finding, if proven to be consistent and repeatable, might lead to the design of new techniques to detect gas bursts. In addition, we have described a method to calculate the bulk dielectric permittivity of the soil, and the volumetric fractions of the soil constituents based on a mixing model. This is valuable information for the geology experts aiming to understand the mechanisms that trigger the emissions of methane from the soil.

While these results are very promising, there is still a lot of room for improvement. The improvements can be made at several levels, e.g., measurement setup, measurement equipment, algorithms for data analysis and modeling assumptions. In the list below, we specify some topics
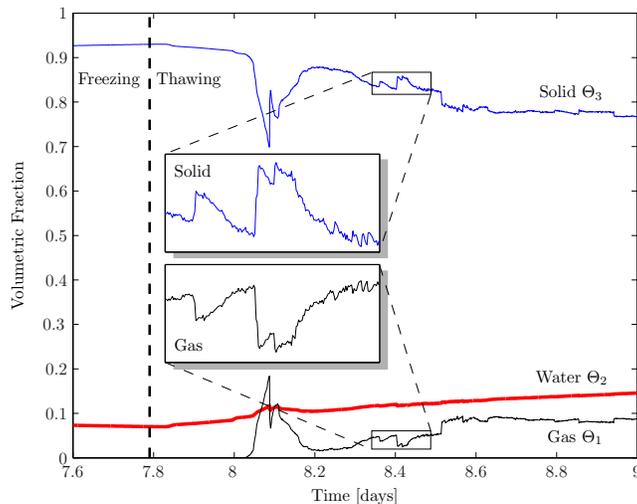
Figure 11: Calculated volumetric fractions as a function of time at 2.28 GHz. The detail plots are given for the same time window as Fig. 10, from day 8.34 to day 8.49.

which can be the basis of future work:

- Our method to calculate the dielectric constant was shown to underestimate the attenuation (i.e., the imaginary part ε'') when measuring pure water, cf. Fig 1. Hence, new methods can be developed, and these should be also validated against materials with well known dielectric properties such as water. In this topic, the approach used in [11] should also be taken into account.

- In this work we only make use of the transmission coefficients, Eq. (1). The reflection coefficients, Eq. (2), also carry valuable information which can be included in the calculations of the dielectric constant.

- The method to calculate the dielectric constant can be further improved by using the information of the whole bandwidth simultaneously, instead of dividing the bandwidth in small sub-bands.

- The processing time of the presented results was rather long since the calculations were based on grid searches, and these are very heavy computationally. However, since the error surface within the considered bounds is convex, see Fig. 5, it should be possible to use iterative algorithms that converge to the solution within these bounds.

The findings of this work have prompted an immediate interest for future work by the all the participants. As a result of that, new spiral antennas have already been designed specially for the propagation in high permittivity mediums as wet soils, and a complete soil monitoring system has been created and transported to Zackenberg, Greenland, where it will be measuring real soil samples from September to November 2009, during the onset of freezing. The study of the data collected in Greenland will be the natural extension of this work. A recent photo of Zackenberg Valley showing the designed antennas buried in the soil and the microwave measurement device, is given in Fig. 12.

15

Figure 12: Photo of Zackenberg Valley in Greenland, taken on August 25th, 2009. The microwave measurement device is a Rohde&Schwarz FSH4 Handheld Network Analyzer.

7 Acknowledgements

References

[1] O. A. Anisimov, "Potential feedback of thawing permafrost to the global climate system through methane emission," *Environmental Research Letters*, vol. 2, no. 4, Nov. 2007.

[2] D. J. Wuebbles and K. Hayhoe, "Atmospheric methane and global change," *Earth-Science Reviews*, vol. 57, no. 3-4, pp. 177 – 210, May 2002.

[3] M. Mastepanov, C. Sigsgaard, E. J. Dlugokencky, S. Houweling, L. Ström, M. P. Tamstorf, and T. R. Christensen, "Large tundra methane burst during onset of freezing," *Nature*, vol. 456, no. 7222, pp. 628–630, Dec. 2008.

[4] A. M. Nicolson and G. F. Ross, "Measurement of the intrinsic properties of materials by time-domain techniques," *IEEE Trans. Instrum. Meas.*, vol. 19, no. 4, pp. 377–382, Nov. 1970.

[5] M. T. Hallikainen, F. T. Ulaby, M. C. Dobson, M. A. El-Rayes, and L.-K. Wu, "Microwave dielectric behavior of wet soil – part I: Empirical models and experimental observations," *IEEE Transactions on Geoscience and Remote Sensing*, vol. GE-23, pp. 25–34, Jan. 1985.

[6] E. H. Kansson, A. Amiet, and A. Kaynak, "Dielectric characterization of conducting textiles using free space transmission measurements: Accuracy and methods for improvement," *Synthetic Metals*, vol. 157, no. 24, pp. 1054 – 1063, Dec. 2007.

[7] K. Lichtenecker, "Dielectric constant of natural and synthetic mixtures," *Phys. Z*, 1926.

[8] Z. Tarik, L. Jean-Paul, and V. Michel, "Theoretical evidence for 'Lichtenecker's mixture formulae' based on the effective medium theory," *Journal of Physics D: Applied Physics*, vol. 31, no. 13, pp. 1589–1594, 1998.

[9] P. Debye, *Polar Molecules*. Chemical Catalog Co. New York (reprinted by Dover, New York, 1954), 1929.

[10] J. O. Curtis, "A durable laboratory apparatus for the measurement of soil dielectric properties," *IEEE Transactions on Instrumentation and Measurement*, vol. 50, no. 5, pp. 1364–1369, Oct. 2001.

[11] A. Muqaibel, "Characterization of ultra wideband communication channels," Ph.D. dissertation, Virginia Polytechnic Institute and State University, 2003.

[12] D. Ballo, "Network analyzer basics – Back to basics seminar," Hewlett-Packard, 1998.

[13] N. Pirk, "Methane emission peaks from permafrost environments: Using ultra-wideband spectroscopy, sub-surface pressure sensing and finite element solving as means of their exploration," Master's thesis, Department of Physical Geography and Ecosystems Analysis, Lund University, June 2009.